Design and Development of a Low-Cost Test-Bed for Undergraduate Education in UAVs

D. Jung, E. J. Levy, D. Zhou, R. Fink, J. Moshe, A. Earl, and P. Tsiotras

***Abstract*— This article describes the efforts undertaken at the School of Aerospace Engineering at the Georgia Institute of Technology for the development of a low-cost Unmanned Aerial Vehicle (UAV) test-bed for educational purposes. The objective of this test-bed is to provide an avenue for the involvement of undergraduate students (primarily) and graduate students (secondarily) in UAV research. The complete design and development of all hardware interfaces of the UAV platform including the on-board autopilot is presented. Based on flight test data a linear model has been developed for the lateral and longitudinal dynamics.**

I. Introduction

UAVs increasingly find their way to applications especially in military and in law enforcement (e.g., reconnaissance, remote delivery of urgent equipment/material, resource assessment, environmental monitoring, battlefield monitoring, ordnance delivery, etc [1], [2], [3]). This trend will only continue in the future, as UAVs are poised to replace the human-in-the-loop airplanes during dangerous missions. Civilian applications of UAVs are also envisioned (crop dusting, geological surveying, search and rescue operations, etc).

Control of unmanned aerial vehicles requires increased automation beyond those encountered in traditional airborne control systems. In order to accomplish complex missions and tasks, UAVs require more advanced navigation and guidance capabilities [4], [5], [6]. The autonomous operation of UAVs requires both trajectory design (planning) and trajectory tracking (control) tasks to be completely automated. Because of the stringent operational requirements and the restrictions imposed on UAVs by autonomy, safety and efficiency, the design of a UAV is truly an interdisciplinary undertaking. It requires methodologies borrowed from aerospace engineering, electrical engineering, communications, operations research, computer science, control systems, real-time operating systems, artificial intelligence, and others. Acquiring these skills mandates a "system's" approach to UAV design. One way to develop such interdisciplinary skills for the next generation of engineers is to promote research-oriented educational projects focusing specifically on UAV technologies. This realization has led several universities to establish research and educational projects to support UAV development [7], [8], [9], [10], [11]. This article presents the activities for the development of a low-cost UAV test-bed at the Guggenheim School of Aerospace Engineering at Georgia Tech.

D. Jung, D. Zhou and E. J. Levy are graduate students at the Guggenheim School of Aerospace Engineering, Georgia Institute of Technology, Atlanta, GA.

R. Fink, J. Moshe and A. Earl are undergraduate students at the Guggenheim School of Aerospace Engineering, Georgia Institute of Technology, Atlanta, GA.

P. Tsiotras is a Professor at the Guggenheim School of Aerospace Engineering, Georgia Institute of Technology, Atlanta, GA. Corresponding author. Email: p.tsiotras@ae.gatech.edu.

Fig. 1. The Goldberg Decathlon ARF model airplane; from [14].

Several autopilot products are already commercially available [12], [13]. These products enable the user to accomplish several tasks, such as autonomous flight control, guidance, waypoint navigation, etc. However, these products provide limited access to the internal control structures. Hence, they are most appropriate for "higher level" control tasks. In order to provide maximum flexibility in control law development and implementation, as well as to maximize the learning experience for the students involved in the project, we have opted to develop both the hardware and the low-level and high-level software in-house. To minimize cost, the UAV platform is based on a commercially available model R/C airframe (Goldberg Decathlon ARF) shown in Fig. 1. The heart of the UAV platform is its autopilot, which consists of a flight control computer, sensors, actuators, communication devices and peripherals, along with the associated software. In the sequel we describe the UAV system architecture, the autopilot hardware components and the subsystem integration process. Details from the sensor calibration and hardware verification through experiments are also provided. We also provide the results from a time domain system identification algorithm utilizing recorded flight test data.

II. UAV Development

A. System Architecture

The overall architecture of the UAV system is shown in Figure 2. The main subsystems are the autopilot, the ground station, and the interconnection between the two. The on-board autopilot is equipped with a micro-controller, sensors and actuators, along with the communication devices that allow full functionality for autonomous control. The micro-controller provides data acquisition, processing, and communication with the ground station. It also runs the main control software. The on-board sensors include angular rate sensors for three axes, accelerometers for three-axes, a three-axis magnetic compass, a GPS sensor, an engine RPM sensor, absolute and differential pressure sensor, battery voltage and fuel level and temperature sensors.

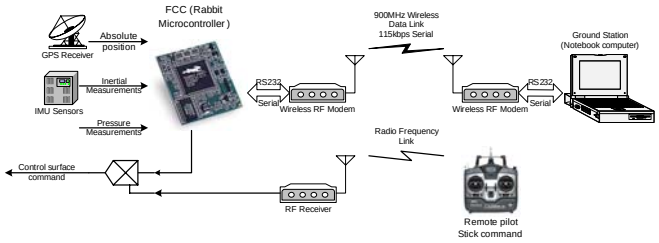

Fig. 2. Hardware system configuration schematic.

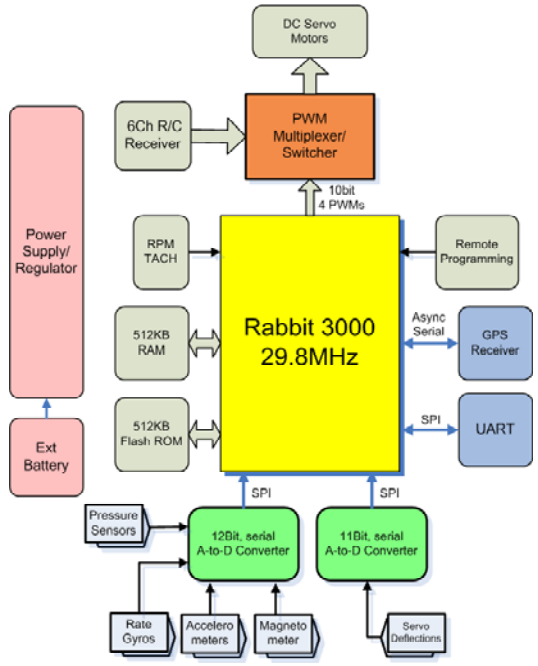

Fig. 3. Sensor board functional block diagram.

B. Autopilot

The autopilot box contains all hardware components, such as the micro-controller, all sensor ICs, signal conditioning circuitry, data acquisition devices, and the wireless modem board.

1) Sensor Board: The microprocessor, sensors and associated electronics were integrated on a custom-designed and fabricated four-layer 5" by 3" printed circuit board (PCB). The sensor board is equipped with three single-chip rate gyros, three two-axis accelerometers, a three-axis magnetometer, two pressure sensors, and a GPS receiver interfacing to the micro-controller module. It also includes the power regulating circuitry that supplies power for all electronic components. Figure 3 shows the functional diagram of the sensor board and Fig. 4 shows the top view of the completed sensor board with all components assembled.

2) Inertial Sensors: Three ADXRS150 angular rate sensors from Analog Devices provide three-axis body-fixed angular rate measurements. Measurements of linear accelerations in all three-axes are provided by three ADXL202 dual-axis chip accelerometers from Analog Devices. A three-axis magnetometer module HMC2003 from Honeywell Solid State Electronics Center (SSEC) is employed to obtain absolute orientation angles with respect to the Earth by sensing Earth's magnetic field. A GPS receiver (Motorola

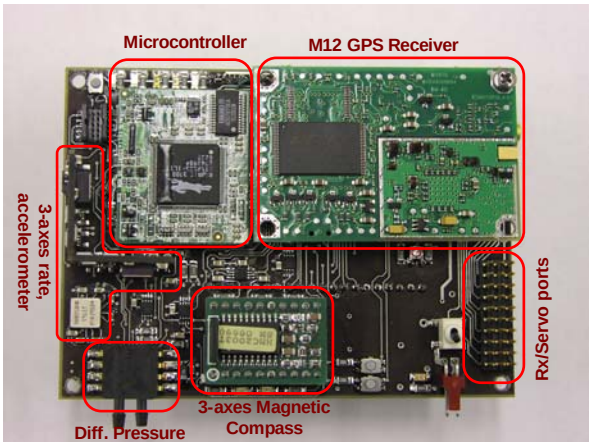

Fig. 4. Assembled autopilot hardware (top view).

OnCore M12) has been used to provide absolute position of the airplane in the Earth-fixed Earth-centered (EFEC) coordinate frame. The output data of the GPS sensor is directly connected to a serial port on the micro-controller using the standard NMEA format or Motorola's native binary format at a rate of 1 Hz.

3) Other Sensors: A MPXV5004D differential pressure sensor that can measure pressures up to 3.92 kPa was used in conjunction with a custom-made pitot-tube, attached under the left wing to obtain airspeed. The altitude of the airplane is obtained from the pressure differential between the ground level and the airplane during flight measured via an MPXAZ4115 pressure sensor.

Engine thrust can be approximately calculated from the knowledge of the engine RPM. The engine RPM is measured by attaching two very small magnets (1/4" diameter) on the back plate of the spinner, and by using a non-contact hall-effect sensor that is fixed on the cowling of the airplane. The hall sensor generates electrical pulses whenever the magnet passes in front it as the propeller spins. By measuring the time interval between each pulse the micro-controller can calculate the engine/propeller speed with a resolution of 1 rpm.

The airplane's control surfaces are actuated with the help of a series of PWM motors. TO obtain command input information for model identification purposes we would like to have accurate knowledge of the deflection angles of all the aerodynamic surfaces (elevator, rudder, ailerons) as well as the throttle setting. These are obtained by measuring the voltage of the potentiometer inside each of the DC servo motors. This approach allows to measure the control surfaces deflections with a resolution of 0.5 deg. Details from the calibration of the DC servo motor potentiometers are given in Section III-C.

Table I summarizes the specifications, operational range, resolution, and noise performance of the autopilot sensors.

4) Communication Modem: The UAV has two main remote communication links (a third, independent link which is used to provide live video feed is not described here). The first link (RF band) uses the standard communication channel between the remote control (Futaba) and the airplane. The second link provides the main data communication backbone between the airplane and the ground station (see Section II-C). These two links are kept completely separate for safety

TABLE I

SENSOR SPECIFICATIONS OF AUTOPILOT SENSORS.

Sensors	Range	Resolution	1-σ noise
Accelerometer	$\pm$2 g	0.004 g	0.025 g
Rate gyro	$\pm$150 °/sec	0.1 °/sec	0.4 °/sec
Magnetometer	$\pm$2 gauss	1.22 mgauss	4 mgauss
Absolute pressure	Above sea level	2.75 m	3 m
Differential pressure	79.2 m/sec	1.40 m/sec	1.5 m/sec
Servo Position	$\pm$60 deg	0.5 deg	

reasons. A Spectra 910 wireless modem was utilized to set up a data communication link between the autopilot and the ground station. The Spectra 910 operates in the license-exempt 900 MHz frequency band utilizing frequency-hopping spread-spectrum, and is capable of providing reliable wireless data transfer up to distance of 25 miles LOS under ideal conditions (at maximum transmitting power). The interface with the micro-controller is achieved via a standard RS-232 serial connection at a maximum baud rate of 115200 bps.

5) Servo Motor Control: The micro-controller has four independent PWM outputs that generate reference command to the motors in pulse form with a varying pulse width according to the desired position. The frequency of the pulse was identified to be 75 Hz, and the duty-ratio (the ratio between [On] time versus [Off] time of the pulse) changes from 5% to 15% for the maximum allowable positions in positive and negative direction, respectively.

To achieve seamless integration (as well as switching back and forth) between autopilot and remote control action the native signal commands from the R/C receiver are merged with the PWM generated output from the micro-controller using a multiplexer. Switching of the multiplexer is being toggled by the remote pilot using a switch on the Futaba transmitter.

C. Ground Station

The ground station consists of a laptop computer with a wireless communication modem. The laptop runs a Windows-based Graphical User Interface (GUI) program developed in-house, shown in Fig. 5. The ground station program provides real-time flight information by displaying all relevant system parameters, sensor readings, etc. A graphical dashboard representing a virtual horizon, altitude and speed has been adopted in the GUI panel to show graphically all information. A map of the area of the UAV's operation can be overlaid on the map panel in order to provide the user with the navigational details of the airplane via GPS data. The ground station program is also capable of coordinating the autonomous flight of the airplane by providing high level navigation control command via way-points on the map specified by the operator.

III. HARDWARE EVALUATION/CALIBRATION

A. Inertial Sensor Calibration

A static test was performed to determine the initial biases and the static noise level of each sensor. The sensor outputs were measured while the autopilot was completely stationary, and by performing a statistical analysis on the recorded data over time, the initial biases and 1-σ noise levels were obtained. The static noise characteristics of all sensor

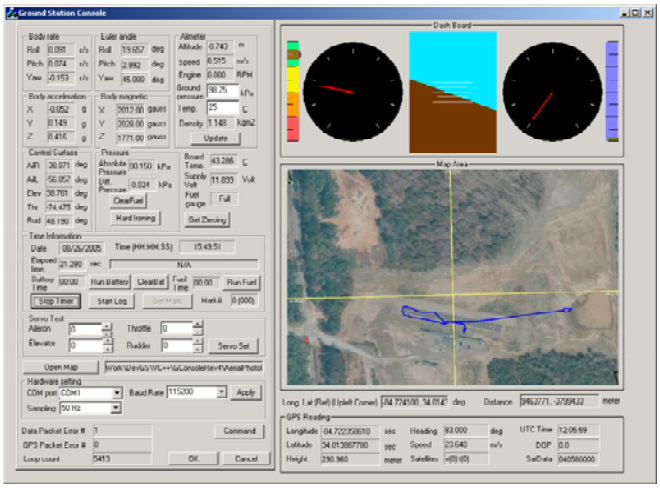

Fig. 5. The ground station GUI program.

correlated favorably with the specification provided by the sensor manufacturer, and summarized in Table I.

The actual scale factors for each accelerometer can be found by taking two measurements with the accelerometer's measurement axis pointed directly towards (+1g) or opposite (-1g) to the Earth. The scale factors can then be found from the difference of two measurements factored by the known gravity change (2g).

The scale factors of the angular velocity sensors were found by placing the autopilot on a three-axis rotational platform [15]. The platform is equipped with a high-performance angular rate gyro and an inertial measurement unit (IMU) capable of measuring angular velocities and linear accelerations in all three-axes with an accuracy better than 0.03 deg/sec, and 0.001 g, respectively. After the autopilot was securely mounted on the platform, the platform was set in motion while both signals from the autopilot and from the high-performance platform sensors were recorded. The rate sensor outputs were then compared, and a least squares fit was employed to find the best scale factor of the autopilot rate sensors. Figure 6 shows the result from this approach. Figure 7 shows the validation of estimated scale factors and biases for the accelerometers on this platform. From the plots, it is asserted that the correlation between the two sets of signals is satisfactory for our purposes.

B. Magnetometer Calibration

The magnetometer can provide absolute orientation and it is not affected by motion constraints. On the other hand, it is susceptible to magnetic disturbances from nearby permanent magnets or ferrous materials that locally distort the Earth magnetic field. Magnetic distortion can be categorized as hard iron or soft iron effects [16]. These effects become evident as the magnetometer is rotated in the horizontal plane. By plotting the two measured signals in the body-axis system, the hard iron distortion appears as a shift of the origin in the phase plot (X_h vs. Y_h), whereas soft iron effects appear as a distortion of a circle to an ellipse in the X_h vs. Y_h plane. Figure 8 shows the hard and soft iron distortions and the compensated magnetometer outputs.

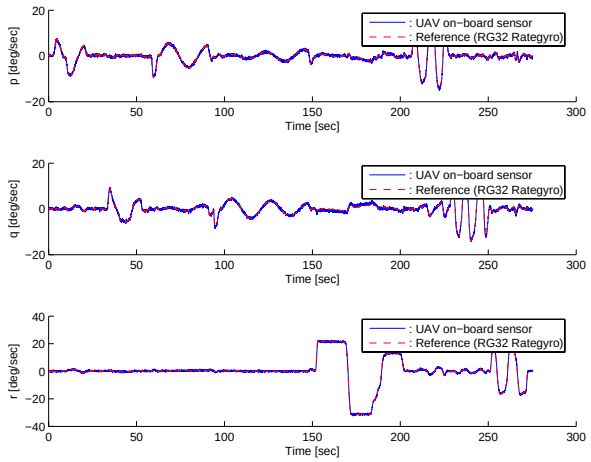

Fig. 6. Angular rate calibration results.

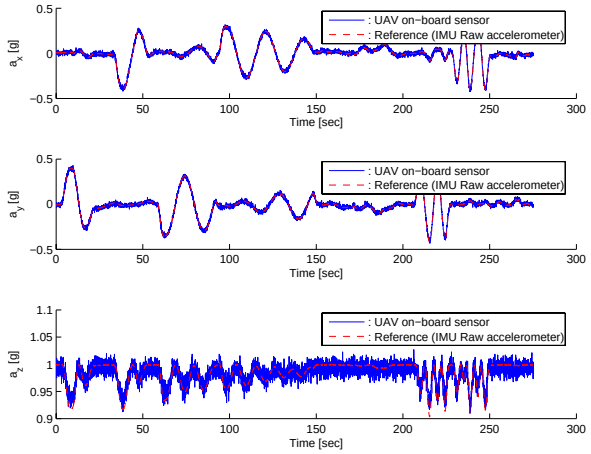

Fig. 7. Accelerometer calibration results.

C. Control Surface Deflection Calibration

One can get the actual angle of the servo motor from the corresponding voltage level of the internal potentiometer of the DC servo motors. Therefore, the deflection angles for each control surface can be determined from each servo's position. An angle meter was used to set the actual deflection angles by a specific amount, while measuring the voltage output from the potentiometer. After several commands were applied to the servo motor, the conversion factor from potentiometer voltage level to actual deflection angle for each control surface was found. In addition, the maximum allowable deflections for each control surface were determined experimentally as well. The results are summarized in Table II.

TABLE II
MAXIMUM DEFLECTION ANGLES FOR EACH CONTROL SURFACE.

Control surface	+Range	-Range
Aileron δ_a	21.8 deg	-18.8 deg
Elevator δ_e	28 deg	-29 deg
Rudder δ_r	15.9 deg	18.3 deg
Throttle δ_T	Full open	Full closed

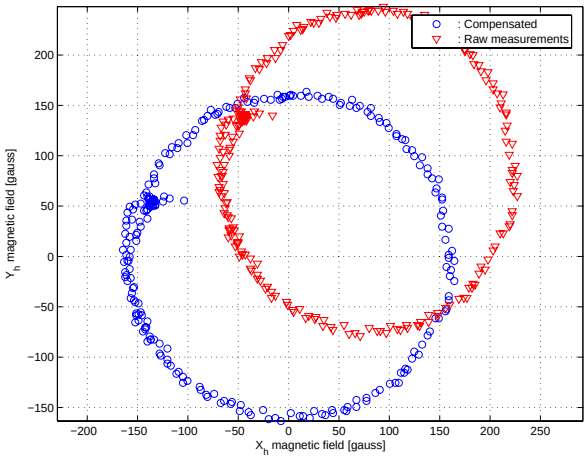

Fig. 8. Effect of hard and soft iron disturbances and compensated magnetometer measurements.

IV. System Identification

Linear models for both the longitudinal and lateral dynamics were derived by applying a time domain system identification algorithm using actual data obtained from a flight test.

A. Linear model

The theoretical linear time-invariant longitudinal dynamics are given by [17],

$$E_1\dot{x}_1 = A_1x_1 + B_1u_1 \tag{1}$$

where the state vector x_1 and the input u_1 are defined by $x_1 = [\Delta\alpha \quad \Delta q \quad \Delta v_T \quad \Delta\theta]^T$, $u_1^T = [\Delta\delta_e \quad \Delta\delta_t]^T$ and

$$A_1 = \begin{bmatrix} Z_\alpha & V_T + Z_q & Z_V - X_{T_V}\,\mathrm{s}\alpha_e & -g\,\mathrm{s}\gamma_e \\ M_\alpha + M_{T_\alpha} & M_q & M_V + M_{T_V} & 0 \\ X_\alpha & 0 & X_V + X_{T_V}\,\mathrm{c}(\alpha_e + \alpha_T) & -g\,\mathrm{c}\gamma_e \\ 0 & 1 & 0 & 0 \end{bmatrix}$$

$$B_1 = \begin{bmatrix} Z_{\delta_e} & -X_{\delta_t}\,\mathrm{s}(\alpha_e + \alpha_T) \\ M_{\delta_e} & M_{\delta_t} \\ X_{\delta_e} & X_{\delta_t}\,\mathrm{c}(\alpha_e + \alpha_T) \\ 0 & 0 \end{bmatrix}, \quad E_1 = \begin{bmatrix} V_T - Z_{\dot\alpha} & 0 & 0 & 0 \\ -M_{\dot\alpha} & 1 & 0 & 0 \\ 0 & 0 & 1 & 0 \\ 0 & 0 & 0 & 1 \end{bmatrix} \tag{2}$$

For the linear lateral dynamics,

$$E_2\dot{x}_2 = A_2x_2 + B_2u_2 \tag{3}$$

where the state vector x_2 and the input u_2 are defined by $x_2 = [\Delta\beta \quad \Delta\phi \quad \Delta p \quad \Delta r]^T$, $u_2 = [\Delta\delta_a \quad \Delta\delta_r]^T$ and

$$A_2 = \begin{bmatrix} Y_\beta & g\,\mathrm{c}\theta_e & Y_p & Y_r - V_T \\ 0 & 0 & \mathrm{c}\gamma_e/\mathrm{c}\theta_e & \mathrm{s}\gamma_e/\mathrm{c}\theta_e \\ L'_\beta & 0 & L'_p & L'_r \\ N'_\beta & 0 & N'_p & N'_r \end{bmatrix}$$

$$B_2 = \begin{bmatrix} Y_{\delta_a} & Y_{\delta_r} \\ 0 & 0 \\ L'_{\delta_a} & L'_{\delta_r} \\ N'_{\delta_a} & N'_{\delta_r} \end{bmatrix}, \quad E_2 = \begin{bmatrix} V_T & 0 & 0 & 0 \\ 0 & 1 & 0 & 0 \\ 0 & 0 & 1 & 0 \\ 0 & 0 & 0 & 1 \end{bmatrix} \tag{4}$$

Note that all states and control inputs are perturbed representations from steady-state (trim) flight condition, where the trimmed angle of attack and flight path angle are given by α_e and γ_e, respectively.

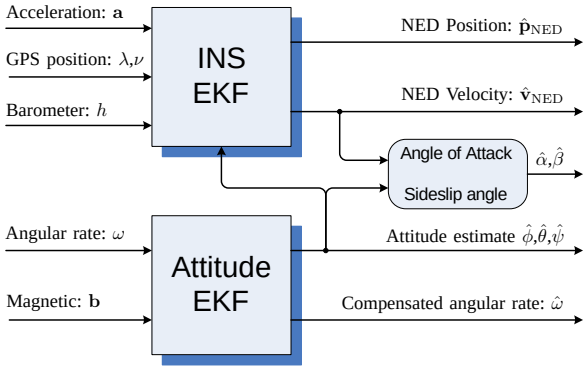

Fig. 9. Cascaded Extended Kalman Filter implementation

B. Theoretical model from airplane's geometry

The linear models shown in Eq. (1) and (3) are formulated using the stability derivatives of the airplane at a certain flight condition. In general, most of these derivatives can be obtained from extensive wind tunnel tests. Alternatively, several of the stability and control derivatives can be computed from the airplane's geometry and mass properties [18], [19]. To this end, precise measurements of the airplane's geometry were taken and a detailed 3D model of the airplane was built in order to estimate its mass and inertia properties. These mass properties and geometric information were used as inputs in a MATLAB® code [20] to estimate all the stability and control derivatives, and from these to build the state space model matrices shown in Eq. (2) and (4). These values then served as an initial guess for the identification algorithm of Sec. IV-D.

C. Extended Kalman filter implementation

An Extended Kalman Filter (EKF) was designed to deal with the inertial sensors' biases and noise, as well as to estimate the angle of attack and the sideslip angles. The EKF was implemented by augmenting the auxiliary states for sensor biases in combination with complementary sensor outputs from the magnetometer (for orientation), the barometer (for altitude), and the GPS receiver (for navigation position). Figure 9 illustrates the schematic of the EKF for estimating the states of the system. The details of the EKF design will be reported in a forthcoming paper.

D. Time domain system identification algorithm

A nonlinear constrained optimization algorithm was used to refine the theoretical model based on recorded flight data. First, certain elements of the state-space matrices were fixed to their known values. The remaining elements were bounded above and below in order to guarantee that the identified model is consistent with the desirable range of the stability derivatives.

The performance criterion during the identification process was given by

$$\mathcal{J} = \sum_{i=1}^{4} \frac{\|y_i - \hat{y}_i\|}{\|y_i - \bar{y}_i\|} \tag{5}$$

where, y_i is the ith ($i = 1, 2, 3, 4$) measured output, $\hat{y}_i$ is the simulated output of the model, and $\bar{y}_i$ is the average of the measured output over the time interval of optimization.

E. Identification results from the experimental data

During the flight test, the airplane was remotely piloted and brought to a trimmed flight condition at a certain throttle setting. Several pre-determined manual inputs, such as aileron doublet, elevator doublet, and rudder doublet were applied by the pilot while holding the other control surfaces close to constant. Figure 10 shows two instances of the test inputs of elevator doublet (upper) and aileron doublet (lower).

During the flight test the autopilot operated solely as a data logger, acquiring measurements from all sensors and down-linking them to the ground station. A wireless data communication was established attaining a packet rate of 50 Hz (one packet consists of all sensor measurements through A/D converter). The maximum data rate of the GPS receiver was set to 1 Hz providing the navigation position in North-East-Down (NED) frame, the two-dimensional speed vector, heading angle, etc.

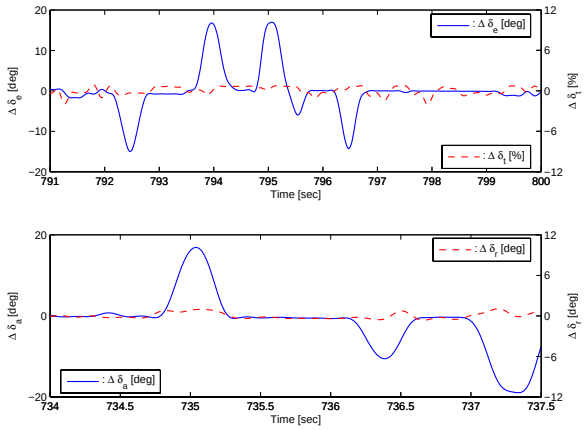

Fig. 10. Inputs of the Longitudinal (upper: $\Delta\delta_e$,$\Delta\delta_t$) and Lateral (below: $\Delta\delta_a$, $\Delta\delta_r$) channels.

Figure 11 shows the results of the identification for the longitudinal dynamics. The quality of the identification is evaluated by the fitting numbers computed as

$$\left(1 - \frac{\|y_i - \hat{y}_i\|}{\|y_i - \bar{y}_i\|}\right) \times 100\% \quad , i = 1, 2, 3, 4 \tag{6}$$

over the interval of interest. In Fig. 11 the solid line represents the measured signal, the dashed-dot line is the simulated output of the theoretical model obtained in Sec. IV-B and the dashed line represents the simulated output of the identified model driven by the same commands as in the flight test. Table III compares the longitudinal modes obtained from the theoretical model with the modes obtained from the identified model.

The identification results for the lateral dynamics are shown in Fig. 12. The identified model fits the experimental data with acceptable accuracy.

Table IV compares the lateral modes obtained from the theoretical model with the modes obtained from the identified model.

V. Conclusions and Future Work

In this article, we have summarized the efforts undertaken by a small group of undergraduate and graduate students at the Guggenheim School of Aerospace Engineering at

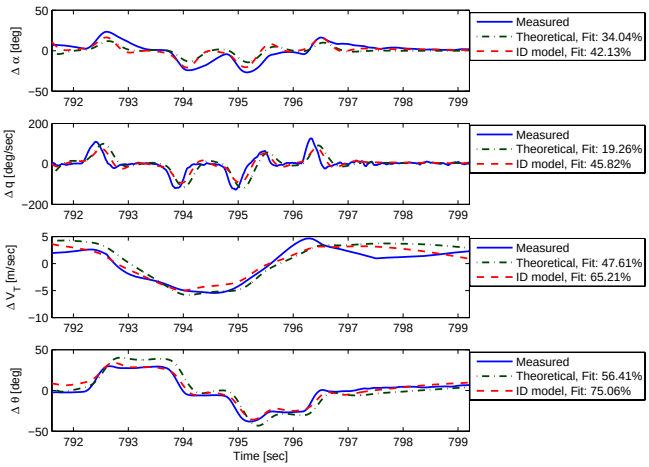

Fig. 11. Longitudinal model identification results.

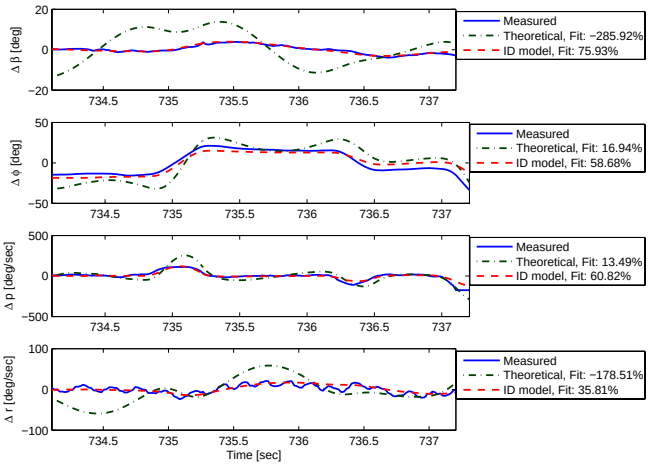

Fig. 12. Lateral model identification results.

Georgia Tech to design and build a low-cost autopilot for a small UAV. The main purpose of this UAV test-bed is to provide an incentive for the involvement of students in UAV-related research and education. The focus from the very start has been to design and assemble as much of the hardware and electronics in house as possible. This choice was opted for in order to maximize the students' learning experience. Details from the calibration of the hardware components have been presented as well as from the development of theoretical linear models for the UAV dynamics. Future work will focus on the design of control algorithms for the autopilot.

Acknowledgement: Partial support for this work has been provided by the Georgia Tech President's Undergraduate Research Awards (PURA) program and NSF award CMS-0510259. The authors would like to give thanks to Dr. Ravi Doraiswami at the Packaging Research Center at Georgia Tech for his assistance with the fabrication of the PCB board, and Prof. Isaac Kaminer for providing the MATLAB® code of Ref. [20].

TABLE III

LONGITUDINAL MODEL IDENTIFICATION RESULTS.

Mode/Parameters		Theoretical	Identified
Phugoid	Pole	-0.04±0.46 i	-0.08±0.65 i
	Damping	0.01	0.12
	Frequency [r/s]	0.46	0.66
Short period	Pole	-4.17 ± 6.11 i	-4.13±8.41i
	Damping	0.56	0.44
	Frequency [r/s]	7.39	9.37

TABLE IV

LATERAL MODEL IDENTIFICATION RESULTS.

Mode/Parameters		Theoretical	Identified
Spiral	Pole	0.01	-0.018
Dutch roll	Pole	-0.17 ± 4.27 i	-0.90 ± 2.93 i
	Damping	0.04	0.29
	Frequency [rad/s]	4.28	3.06
Pure roll	Pole	-14.6	-38.1

REFERENCES

[1] P. Chandler and M. Pachter, "Research issues in autonomous control of tactical UAVs," in *Proceedings of the American Control Conference*, Philadelphia, PA, 1998, pp. 394–398.

[2] R. Prasanth, J. Bošković, S.-M. Li, and R. Mehra, "Initial study of autonomous trajectory generation for unmanned aerial vehicles," in *Proceedings of the 40th IEEE Conference on Decision and Control*, Orlando, FL, 2001, pp. 640–645.

[3] T. McLain, P. Chandler, and M. Pachter, "A decomposition strategy for optimal coordination of unmanned air vehicles," in *Proceedings of the American Control Conference*, Chicago, IL, 2000, pp. 369–373.

[4] S. Twigg, A. Calise, and E. Johnson, "On-line trajectory optimization for autonomous air vehicles," in *AIAA Guidance, Navigation, and Control Conference*, Austin, TX, 2003, pp. AIAA 2003–5522.

[5] J. Bellingham, A. Richards, and J. How, "Receding horizon control of autonomous aerial vehicles," in *Proceedings of the American Control Conference*, Anchorage, AK, 2002, pp. 3741–3745.

[6] S. A. Bortoff, "Path planning for UAVs," in *Proceedings of the American Control Conference*, Chicago, IL, 2000, pp. 364–368.

[7] E. Hallberg, I. Kaminer, and A. Pascoal, "Development of the rapid flight test prototyping system for unmanned air vehicles," in *Proceedings of the American Control Conference*, Philadelphia, PA, June 1998, pp. 699–703.

[8] D. Kingston, R. W. Beard, T. McLain, M. Larsen, and W. Ren, "Autonomous vehicle technologies for small fixed wing UAVs," in *2nd AIAA Unmanned Unlimited Conference and Workshop and Exhibit*, Chicago, Illinois, Sept. 2003, paper AIAA-2003-6559.

[9] D. B. Kingston and R. W. Beard, "Real-time attitude and position estimation for small UAVs using low-cost sensors," in *AIAA 3rd* Unmanned Unlimited *Technical Conference, Workshop and Exhibit*, Chicago, IL, Sept. 2004, paper AIAA 2004-6488.

[10] J. Jang and C. Tomlin, "Longitudinal stability augmentation system design for the DragonFly UAV using a single GPS receiver," in *AIAA Guidance, Navigation, and Control Conference*, Austin, TX, 2003, pp. AIAA 2003–5592.

[11] D. H. Shim, H. J. Kim, and S. Sastry, "Control system design for rotorcraft-based unmanned aerial vehicles using time-domain system identification," in *Proceedings of the 2000 IEEE International Conference on Control Applications*, Anchorage, AK, 2000, pp. 808–813.

[12] (2004) Micro Pilot. Stony Mountain, Canada. [Online]. Available: http://www.micropilot.com

[13] (2004) Cloud Cap Technologies. Hood River, OR. [Online]. Available: http://www.cloudcaptech.com

[14] (2004) Carl Goldberg Products Ltd. Oakwood, GA. [Online]. Available: http://www.carlgoldbergproducts.com/decathlonARF.htm

[15] D. Jung and P. Tsiotras, "A 3-dof experimental test-bed for integrated attitude dynamics and control research," in *AIAA Guidance, Navigation, and Control Conference*, Austin, Texas, 2003, pp. AIAA 2003–5331.

[16] M. J. Caruso, "Applications of magnetoresistive sensors in navigation systemss," Technical article, Honeywell. [Online]. Available: http://www.ssec.honeywell.com/magnetic/datasheets/sae.pdf

[17] B. L. Stevens and F. L. Lewis, *Aircraft Control and Simulation*, 2nd ed. John Wiley & Sons, 2003.

[18] J. Roskam, *Methods for Estimating Stability and Control Derivatives of Conventional Subsonic Airplanes*. Self-published, 1971.

[19] F. O. Smetana, *Computer Assisted Analysis of Aircraft Performance, Stability, and Control*. New York: McGraw-Hill, 1984.

[20] E. J. Watkiss, "Flight dynamics of an unmanned aerial vehicle," Master's thesis, Naval Postgraduate School, Monterey, 1994.